A Frequency-Time Partitioned Approach for Computing Fan Blade Flutter Induced Limit Cycle Oscillations With Nonlinear Friction on Contact Interfaces

Nicolas Ombret, Renaud Daon, Alain Dugeai, Fabrice Thouverez, Laurent Blanc

A FREQUENCY-TIME PARTITIONED APPROACH FOR COMPUTING FAN BLADE FLUTTER INDUCED LIMIT CYCLE OSCILLATIONS WITH NONLINEAR FRICTION ON CONTACT INTERFACES

Nicolas Ombret[1,2,3], Renaud Daon[1], Alain Dugeai[2], Fabrice Thouverez[3], Laurent Blanc[3]

[1]Safran Aircraft Engines, Moissy-Cramayel, France
[2]DAAA, ONERA, Université Paris Saclay, F-92322 Châtillon, France
[3]LTDS, École Centrale de Lyon, Écully, France

ABSTRACT

This paper aims at introducing a new methodology to analyse aeroelastic stability of transonic fans while nonlinear friction on contact interfaces is taken into account. This methodology consists in an iterative procedure where the nonlinear dynamics of the structure and aerodynamic forces are respectively computed while imposing each one to the other in a fixed point loop. Hence, both physics are resolved while taking into account the nonlinearities of the other one, leading to a description of the fully coupled fluid structure system nonlinear dynamics. To do so, a harmonic description of the structure dynamics is performed using nonlinear complex modes, while the fluid is evaluated in temporal domain solving Unsteady Reynolds Averaged Navier-Stokes (URANS) equations. Aeroelastic simulations are performed on the whole annulus, in Arbitrary Lagrangian Eulerian (ALE) formulation. An application of this methodology is performed on an industrial state of the art transonic fan to demonstrate its capability of predicting flutter induced Limit Cycle of Oscillations (LCO).

Keywords: Aeroelasticity, Fan blade flutter, Nonlinear blade root friction, Nonlinear complex modes, Limit Cycle of Oscillations (LCO)

NOMENCLATURE

C	damping matrix
K	stiffness matrix
M	mass matrix
f	force vector
x	displacement
Ψ	modal deformation shape
Z	multiharmonic stiffness matrix
X	harmonic coefficients of displacement
N_h	harmonics number
β	nonlinear damping
ω	frequency
$\bullet_{nl}$	nonlinear component

1. INTRODUCTION

Aeroelastic stability of turbomachinery compressor rows has been studied for decades and is yet not fully understood. In order to achieve fuel consumption reduction objectives sought by engine manufacturers, it has become more and more critical to gain knowledge about the operability limits of such systems to perform dry masses reductions without compromising the lifecycle or the performances of the engine.

In the past decade, the intensive use of Computational Fluid Dynamics (CFD) allowed to get better understanding of physical mechanisms inducing flutter of transonic fan stages. Some studies [1,2,3,4] showed that shock/boundary layer interaction is a key mechanism inducing energy transfer between the fluid and the structure in such operating conditions. This interaction may lead to boundary layer separation, resulting in positive energy transfer areas from the fluid to the blades, hence instability. This phenomenon is often referred as transonic stall flutter in compressor applications [5]. Another key mechanism of fan blade flutter has been revealed more recently and is due to inlet fan acoustic interactions [2,4,6,7]. As the latter vibrates, it may be at the origin of acoustic waves propagating through the intake of the engine. The propagation of such acoustic waves along the duct depends on the mean flow, the intake geometry and the frequency of the source. It is then possible to describe the acoustic propagation in terms of duct acoustic modes, characterized by a cut-on frequency $\boldsymbol{\omega_{cut-on}}$ [8]. In particular, an acoustic mode will propagate through the duct if the source frequency at its origin is greater than $\boldsymbol{\omega_{cut-on}}$, otherwise it will decay. Acoustic reflection occurs at the intake opening, leading to a reflected wave going back to the fan. The relationship between the emitted wave and the reflected one onto the fan may have a great impact on flutter stability in very narrow operating conditions, hence the term flutter bite.

While fan flutter may lead to critical failure of the engine, it has been shown in some studies that nonlinear phenomena may reduce its impact by saturating the vibrating amplitudes of the blades. Firstly discussed on simple models [9], it has been shown on state of the art compressors and turbines that the effects of nonlinear friction on contact interfaces may improve flutter stability by giving rise to periodic oscillations called Limit Cycle of Oscillations (LCO). LCOs occur beyond the stability limits predicted in the scope of a linear structure [10,11,12]. For such systems, nonlinear friction has several effects: first, it leads to energy dissipation in the form of heat, which contributes to the aeroelastic stabilization of the row as the energy provided by the fluid to the structure is dissipated by friction. Secondly, it changes the free dynamics of the system, as it is responsible to a reduction of the free frequency of vibration $\boldsymbol{\omega}$ and changes in its deformation shapes $\boldsymbol{\Psi}$. In the context of fluid structure interactions, such changes may modify the fluid dynamics, and thus the stability of the whole aeroelastic system. The impact of such changes may be even more important in the context of inlet fan acoustic interactions.

In this paper, we are interested in describing the effects of nonlinear friction at blade roots on the aeroelastic stability of a transonic fan. As the free vibration frequency and deformed shape of the blades may differ from their linear dynamics due to blade disk friction, an impact is expected on the energy transfer between the fluid and the structure. The aeroelastic stability is also expected to change as dissipation occurs at blade roots. In order to predict these changes, a new fluid structure coupling methodology using nonlinear complex modes [13,14] is proposed. This methodology is applied on an industrial case to demonstrate its ability to predict flutter induced LCO.

2. DESCRIPTION OF NONCONSERVATIVE AUTONOMOUS SYSTEMS WITH NONLINEAR CONTACT INTERFACES

2.1 Nonlinear Complex Modes

Nonlinear complex modes [13] are a tool allowing describing the free dynamics of a system having some nonlinear contact interfaces. Let us consider a structure discretized according to a finite element formalism. The equation that characterizes its dynamics is the equation (1):

$$M\ddot{x} + C\dot{x} + Kx + f_{nl}(x,\dot{x}) = 0 \qquad (1)$$

where M, C and K are respectively the mass, damping and stiffness matrices of the structure. The displacement vector of the structure is represented by x and f_{nl} is the vector of temporal nonlinear dry friction forces which may depend on the structure displacement and velocity.

By analogy with the free vibration of a damped linear structure, nonlinear complex modes are defined as a decaying multiharmonic expansion of the displacement. If we consider N_h harmonics of motion, it may be written as in equation (2):

$$x = \mathrm{a}_0 + \sum_{k=1}^{N_h}(a_k \cos(k\omega t) + b_k \sin(k\omega t))\, e^{-k\beta t} \qquad (2)$$

As friction nonlinearities depend on vibration amplitudes of the structure, the harmonic coefficients vectors a_k and b_k depend on it as well. Likewise, both nonlinear decay coefficient β and free frequency ω are unknowns which depend on the level of nonlinearities activated in the system. Hence, the more friction appears in the system, the greater is the evolution of these terms.

Under the assumption that there are two different time scales so that $\omega \gg \beta$ is verified, it is possible to express the differential equation (1) into an algebraic one by the means of a Galerkin procedure. The inner product of square integrable complex functions, expressed in equation (3), is used as a scalar product for the Galerkin procedure:

$$\forall f, g \in C^{\mathbb{C}}\left(0; \frac{2\pi}{\omega}\right)^2, \langle f|g\rangle = \frac{\omega}{\pi}\int_0^{2\pi} f(t)\overline{g(t)}dt \qquad (3)$$

whereas the Fourier basis functions are used as projection basis. Equation (1) is then expressed in the frequency domain as follow:

$$Z(\omega,\beta)X + F_{nl}(X,\omega,\beta) = 0 \qquad (4)$$

where the multiharmonic stiffness matrix Z is built from the structural matrices of equation (1).

In equation (4), the unknowns are X (vector containing the harmonic terms a_k and b_k), ω and β. As there are two more unknowns than equations, it is necessary to add two relations to make the problem well posed. Many constraint equations may be used, as they will allow finding solutions with different approaches by setting continuation techniques [15]. Sequential continuation may be the simplest way to perform the continuation, whereas arc-length continuation may be more robust, especially if bifurcations as turning points are expected. To solve equation (4), an initialization of the structure dynamics is mandatory. A convenient way to get this dynamics is to consider the asymptotical linear case where only small vibrations of the structure are reached. Thus, there is not enough energy in the system to trigger friction and the blade root interface stay stuck. A classical Newton-Raphson algorithm allows one to find the nonlinear dynamics of the system [15].

2.2 Aeroelastic stability with nonlinear contact interfaces

In this study, we are interested in adding an external contribution to the nonlinear complex mode formulation. It is expected to represents the aerodynamic forces coming from the free interaction between the fluid and the nonlinear dynamics of the structure. Hence, the updated nonlinear complex mode taking into account aerodynamic forces is sought in the form:

$$Z(\omega,\beta)X + F_{nl}(X,\omega,\beta) = F_a(X,\omega,\beta) \qquad (5)$$

where F_a represents aerodynamic forces applied on the structure in the harmonic domain. As it is a free interaction force, it depends on the structure dynamics, hence its nonlinear movement X, its free frequency ω and possibly the nonlinear decay coefficient β. The main problem is now to get an expression for F_a. To do so, a partitioned coupling approach has been considered in this work, consisting in a strong coupling between a temporal CFD solver and a harmonic Computational Structural Mechanics (CSM) solver to compute nonlinear complex modes.

2.3 Strong coupling strategy: frequency-time partitioned approach

A strong partitioned coupling procedure taking profit of the previously described numerical tool is proposed here, illustrated in FIGURE 1. It consists in a classical fixed point loop between the two solvers respectively computing the nonlinear dynamics of the structure and the one of the fluid. The algorithm is similar to the one used by Berthold *et al.*[12] as part of the extended energy method , apart from the fluid solver which is harmonic in their study while a time accurate solver is considered for the fluid in this work. Another major difference between the two studies is that nonlinear complex modes have been chosen to describe the structure dynamics in the present work instead of a modal representation in accordance with the Extended Periodic Motion Concept [12].

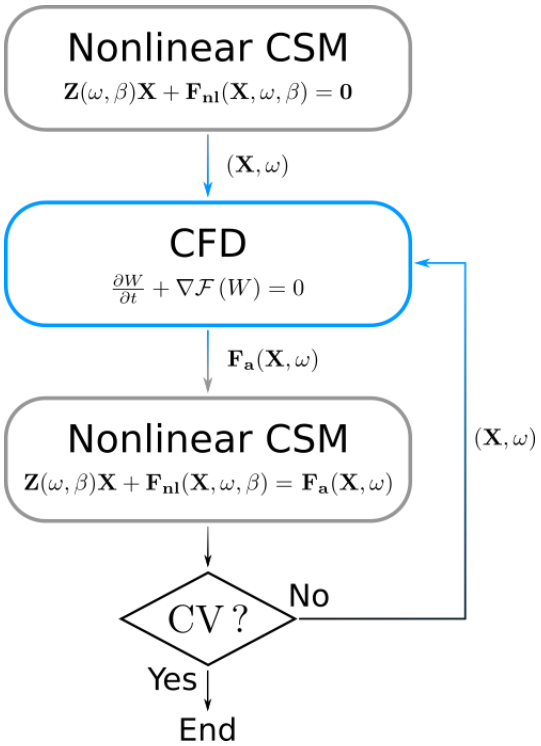

FIGURE 1: STRONG COUPLING PARTITIONED PROCEDURE

First, the nonlinear dynamics of the structure is computed by the use of nonlinear complex modes while the structure is supposed to be in vacuum condition. It is thus a classical computation of nonlinear complex mode, as already described in other studies [13,14]. As the nonlinear dynamics of the structure is energy dependent, there exists a nonlinear deformed shape X and free vibration frequency ω for each energy levels (*i.e* each vibration amplitude). Those quantities change continuously with respect to the energy level in the system.

Then, the nonlinear deformed shape X as well as the free frequency ω are sampled for a chosen set of energy levels leading to a discretization of the nonlinear complex mode with respect to the energy level. Each of these dynamics (X and ω) is imposed to the structure in a time accurate aeroelastic computation, which gives the corresponding aerodynamic forces applied on the structure. The decay coefficient β is not taken into account in this computations as $\omega \gg \beta$. At each period of vibration of the blade, a Fourier analysis is performed on the computed aerodynamic forces to get the corresponding harmonic aerodynamic forces coefficients F_a. These terms are associated with the free nonlinear movement of the blades: they represent the free interaction forces between the fluid and the structure. When a sufficiently high number of period has been reached, one can expect to observe a convergence of the harmonic coefficients F_a. The converged harmonic forces coefficients may then be extracted and used to update the previous nonlinear complex mode in vacuum. The sampled values of F_a are interpolated against the energy levels so they may change continuously during the nonlinear complex mode update described by equation (5). It is particularly convenient when a sequential continuation is employed, as we may set the force-energy dependency law so that F_a is constant for a given value of a control degree of freedom (thus the jacobian remains the same because F_a is constant). In terms of equations, this statement can be written by fixing the amplitude and phase of a certain degree of freedom of a physical node n_{obs}: it is thus assumed that there exists only one energy level for a given amplitude of vibration. For instance, if we choose a null phase for the corresponding degree of freedom, the sequential continuation takes the form of equation (6) where λ stands for a continuation parameter which sets the amplitude of motion.

$$\begin{cases} Z(\omega,\beta)X + F_{nl}(X,\omega,\beta) = F_a(\lambda) \\ a_{k,n_{obs}} = \lambda \\ b_{k,n_{obs}} = 0 \end{cases} \quad (6)$$

When using a sequential continuation in our partitioned approach, it is then considered that F_a is constant for a chosen value of the continuation parameter λ. It is thus not necessary to derive the jacobian of F_a against the structure nonlinear dynamics X and ω since it is constant for a given value of λ. However, it should be kept in mind that sequential continuation may be limited in case of turning point bifurcations. In such cases, other continuation techniques such as arc length continuation may allow performing the computation without trouble, but it would need a derivation of the jacobian of F_a

against X and ω which is not trivial. To the knowledge of the authors, such bifurcations well known for geometrical nonlinearities (Duffing oscillator) does not occur when it comes to dry friction nonlinearities, which led to the choice of sequential continuation.

Once the updated nonlinear dynamics of the structure has been computed, it is possible to repeat this procedure until convergence of the whole nonlinear fluid structure system is reached. In the end, the nonlinear dynamics of the structure is obtained while taking into account free interaction forces between the fluid and the structure. Careful attention must be paid to the conservation of the phase condition between aeroelastic and structural computations: the Fourier analysis of aerodynamic forces must be carried out with the same phase movement as the one supplied by the structural computation. Otherwise, the phase error between the movement and aerodynamic forces will introduce inconsistency between the fluid and the structure, leading to the algorithm failure. It should also be mentioned at this point that the method is meaningful only if the harmonic aerodynamic forces coefficients F_a are converged, meaning that a sufficiently high number of period of vibration are required for all aeroelastic computations. However, there is no rule to determine *a priori* the number of period of vibration to use to ensure the convergence of the coefficients F_a, as it may depend on the considered bladed row, operating point or deformation shape.

3. CASE MODELLING

3.1 Flow solver

The fluid dynamics is characterized by 3D compressible Unsteady Reynolds Averaged Navier-Stokes (URANS) equations, written as:

$$\frac{\partial W}{\partial t} + \overrightarrow{div}.\mathcal{F}(W) = 0 \qquad (7)$$

where W is the vector of conservative variables $(\rho\ \rho U\ \rho E)^T$ and $\mathcal{F}(W)$ the flux vector written as :

$$\mathcal{F}(W) = \begin{pmatrix} \rho U \\ \rho U \otimes U + P.I - \tau \\ \rho E U + P.U - \tau.U + q \end{pmatrix} \qquad (8)$$

In equation (8), P stands for static pressure, τ for the viscous stress tensor and q for the heat flux. We consider the fluid being a perfect gas and its viscosity evolving according to the Sutherland law. The equations are solved using the finite volume solver *elsA* developed at ONERA [16]. Turbulence is modelled using the two equations *k-l* of Smith model [17], while the Roe upwind flux-difference splitting scheme [18] is used with the Van Albada limiter [19] for the fluxes evaluation.

A state of the art fan made of 18 blades provided by Safran Aircraft Engines has been used for this study. An aerodynamic mesh of the whole annulus assembly has been built and is illustrated in FIGURE 2. It is made from two meshes, one for the inlet and the other for the fan, connected to each other upstream of the fan in the intake (red line on FIGURE 2). As the two meshes do not match both radially and azimuthally at the interface, an interpolation of the field is made at each timestep of unsteady computation. The fan mesh does not rotate in the simulations: fan rotation is taken into account by adding source terms in the Navier-Stokes equations in the relative frame linked to the fan mesh.

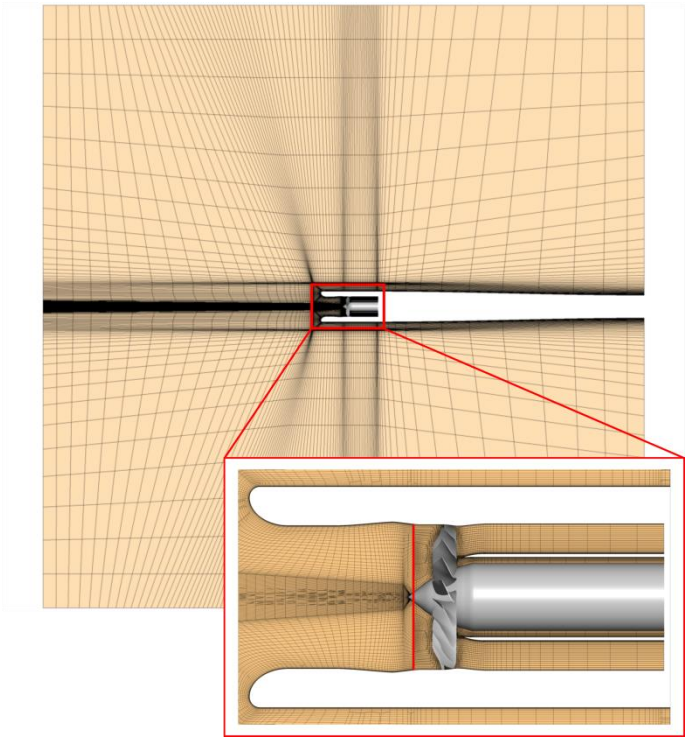

FIGURE 2: SLICE OF THE MESH USED IN *ELSA* SIMULATIONS

The whole mesh has about 11 million cells, with 3 million cells for the intake mesh and 410000 cells per blade passage downstream of the interface. FIGURE 3 illustrates the blade mesh and its tip. As we do not want the boundary conditions to have spurious interactions with possible acoustic waves, a mesh coarsening has been applied outside of the inlet and downstream of the fan with a 1.2 expansion ratio in the axial direction for primary and secondary flows and in all directions outside of the engine. The external domain is thus 30 times greater than the fan diameter.

We are interested in studying aeroelastic stability of the fan at 75% part speed, as it has been seen during experiments that flutter occurred at this speed range near surge. Adiabatic rigid walls are considered for the structure while the fluid being viscous. Static pressure distribution is imposed considering radial equilibrium equations of momentum on primary and secondary outlets, which allows selecting the operating point on the 75% part speed of the fan characteristic. A complete set of conservative variables are imposed on farfield boundaries, allowing to obtain an axial Mach number of 0.1 and standard sea

level conditions (total temperature of 288.15 K and total pressure of 101325 Pa). Unsteady computations are initialized with results obtained from steady computations, and conducted using Dual Time Stepping scheme for the integration in time.

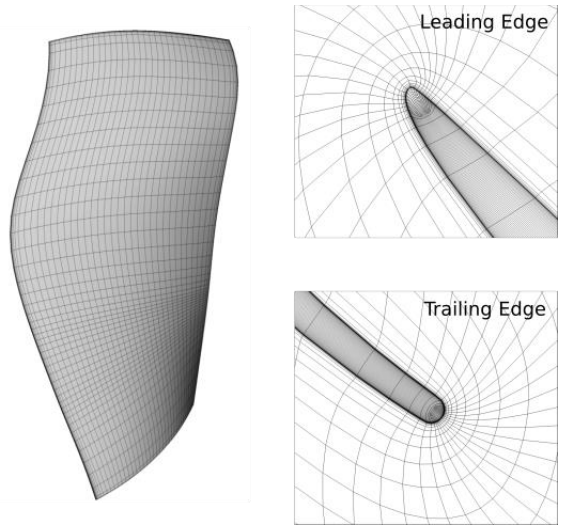

FIGURE 3: MESH DETAILS ON THE BLADE SURFACE AND ITS TIP (*ELSA* SIMULATIONS)

3.2 Aeroelastic model

In this study, aeroelastic computations are done with respect to the Arbitrary Lagrangian Eulerian (ALE) [20] formulation of Navier-Stokes equations while prescribing a predetermined movement to the fan blades.

In classical approaches, a linearization of aerodynamic forces is assumed, allowing to study separately the aeroelastic stability of each structural mode. The structure is deformed according to the studied mode shape at its eigenfrequency, assuming that the aeroelastic system is weakly coupled and that the structure dynamics is not changed by the fluid (except its stability). This method allows building stiffness and damping aerodynamic matrices using the coefficient of influence method [11,21,22]. It has been used in this study in order to predict the stability limit of the fan in the scope of a linear structure. Especially, the first bending mode with 2 and 3 diameters (respectively called 1F2D and 1F3D when considering cyclic symmetry hypothesis) has been studied, as the former has been detected as unstable at 75% part speed near surge while the latter did not.

When the nonlinear dynamics of the structure will be considered using nonlinear complex modes in the scope of the frequency-time partitioned approach, a multiharmonic movement will be imposed to the blade according to the level of amplitude reached by the structure.

Whether the linear or nonlinear dynamics of the structure is employed in the aeroelastic computations, the number of timesteps has been chosen so that 50 vibration periods are achieved and the steady state is reached for each computation. The convergence is checked by looking at the evolution of the generalized aerodynamic forces (resulting from the projection of aerodynamic forces on the modal deflection shapes Ψ) in terms of amplitude and phase during the computation.

3.3 Structural nonlinear model

A finite element model of the fan blade disk sector has been used to build the structural nonlinear model. It involves two distinct parts, the blade on one hand and the disk on the other, with a coincident mesh on the contact interfaces at blade roots. FIGURE 4 illustrates this model.

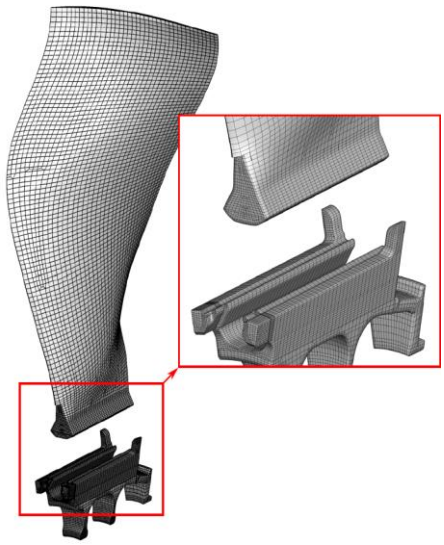

FIGURE 4: FINITE ELEMENT MODEL USED TO BUILD THE NONLINEAR STRUCTURAL MODEL

As the whole blade disk finite element model depicted in FIGURE 4 has a high number of degrees of freedom, reduced order models (ROM) using Craig Bampton (CB) substructuring method [23] has been built for both blade and disk model to perform faster computations. The CB substructuring method consists in expressing the motion in a combination of normal modes with fixed interfaces Ψ_0 and static constraint modes Ψ_C, such as in equation (9).

$$x = \Phi_{CB} x_{CB} \quad \text{with} \quad \Phi_{CB} = \begin{pmatrix} I & 0 \\ \Psi_C & \Psi_0 \end{pmatrix} \qquad (9)$$

15 and 30 normal modes with fixed interfaces have respectively been kept for the disk and blade ROMs, while 180 physical nodes (*i.e* static constrained modes) have been kept at blade root contact interfaces for both models. 125 additional physical nodes have been kept on the blade skin so that the blade movement may be extracted without using the CB matrix Φ_{CB}. A final reduction is applied on the model allowing one to solve the whole nonlinear blade disk dynamics by considering only the relative movement of the substructures on the contact interfaces [24]. Hence, the number of kept linear d.o.f is not relevant in the computational cost of the method as the size of the system to be

solved is determined by the number of nonlinear d.o.f (*i.e* the number of kept nodes at blade roots). The influence of the number of retained modes in the CB ROMs on the coupling strategy has been investigated. However, it is beyond the scope of this work [25] and will be addressed in more details in a further paper.

The ROMs created with the help of CB reduction are used to solve equations (4) and (5). An analysis upon the convergence of the nonlinear complex mode in vacuum against the number of harmonics N_h revealed that 3 harmonics is enough to get a good representation of nonlinear friction forces and thus of the nonlinear dynamics of the structure. Hence, all the results reported in this work regarding nonlinear complex modes have been obtained considering 3 harmonics of motion. Equation (4) is solved to get the structure dynamics in vacuum while equation (5) allows taking into account aerodynamic forces in the computation of the blade nonlinear dynamics. Nonlinear forces are applied on the kept physical nodes at blade roots when creating the ROM. They are computed thanks to the Dynamic Lagrangian Frequency Time method (DLFT) [24] which allows applying exact Coulomb friction laws, without regularization. A natural structural damping is considered on each linear mode of each substructures in the form of a diagonal matrix in the modal subspace. The same damping value of 0.05% is considered for each linear mode.

4. NUMERICAL RESULTS

4.1 Steady computations

Steady computations of the transonic fan have been performed on the 75% part speed characteristic. Normalized results are displayed in FIGURE 5, and may be compared to experimental data. More precisely, the experimental characteristics are the ones obtained for 70%, 74.8% and 80% part speed.

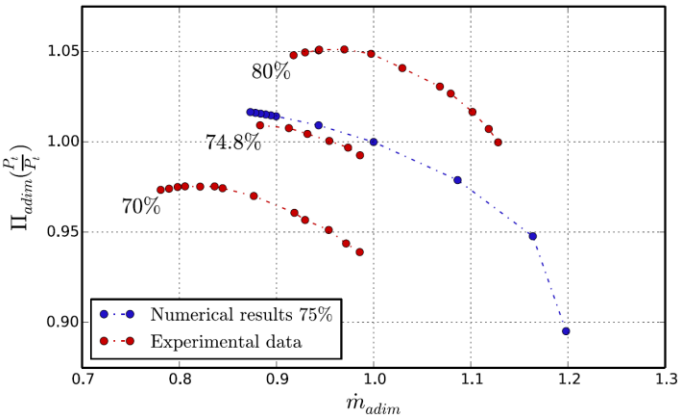

FIGURE 5: NORMALIZED CHARACTERISTICS OF THE STUDIED FAN

A good agreement is observed between steady numerical results and experimental data near stall line. Discrepancies appear between them for higher massflow rates. This may be due to the boundary conditions, which are better suited to representing near stall operating conditions. As we are more interested in working points near stall, we consider that we are sufficiently close to measured data to pursue the study with this model.

For unsteady computations, we are interested in describing the aeroelastic stability of operating points near stall. TABLE 1 sums up which massflow rates were studied on the 75% part speed.

Name	dp19	dp20	dp21	dp22	dp23
$\dot{m}_{adim}$	0.894	0.889	0.884	0.878	0.873

TABLE 1: OPERATING POINTS ON THE 75% PART SPEED FOR AEROELASTIC COMPUTATIONS

The flow topology on the blade pressure and suction sides for the nearest operating point to stall (named dp23 according to TABLE 1), is depicted in FIGURE 6. A colormap of the isentropic Mach number onto the blade may be seen, superimposed with the surface streamlines.

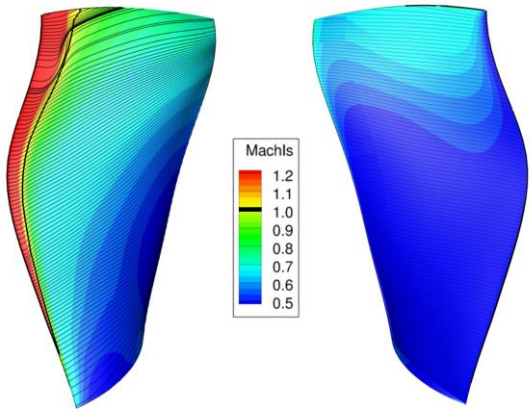

FIGURE 6: ISENTROPIC MACH NUMBER AND SURFACE STREAMLINES ON THE BLADE SUCTION AND PRESSURE SIDES ON DP23 OPERATING POINT

Given by equation (10), the isentropic Mach number represents the Mach number we would have on the blade skin without any loss (*i.e* for an isentropic flow without viscous friction on solid surfaces). P_t^∞ is the total pressure in the farfield, P is the static pressure on blade skin and γ is the specific heat ratio.

$$\mathrm{Mach}_{\mathrm{is}} = \sqrt{\left(\left(\frac{P_t^\infty}{P}\right)^{\frac{\gamma-1}{\gamma}} - 1\right).\frac{2}{\gamma-1}} \qquad (10)$$

The isentropic Mach number in FIGURE 6 shows a strong shock on the blade suction side, close to its leading edge (indicated by the bold black curve). The shock becomes stronger when

approaching the blade tip, as a deviation of the surface streamlines may be observed around 90% blade height. However, no boundary layer separation has been noticed. Still, we will see in the next subsection that the shock plays a major role in the aeroelastic stability of the transonic fan, as it is accompanied by high energy transfer between the fluid and the structure.

4.2 Aeroelastic stability in the scope of a linear structure

As mentioned earlier, the aeroelastic stability of both 1F2D and 1F3D structural linear modes have been studied on the 75% part speed. For a given eigen mode vibrating at amplitude q_0, the aeroelastic stability of the mode may be described by equation (11).

$$\xi_{aero} = -\frac{W}{2\pi\mu\omega_0^2|q_0|^2} \tag{11}$$

ξ_{aero} represents the aerodynamic damping, μ the generalized mass and ω_0 the eigen frequency of the eigen mode. W stands for the work of aerodynamic forces on the blades for a vibration of the considered mode at the amplitude q_0. The aerodynamic damping associated with these modes is illustrated in FIGURE 7, a negative value designating unstable operating conditions (*i.e* the fluid gives energy to the structure).

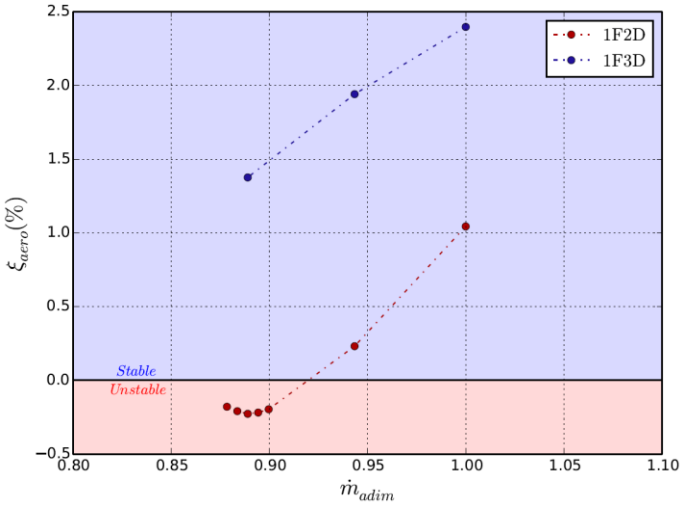

FIGURE 7: AEROELASTIC STABILITY OF 1F2D AND 1F3D MODES ON THE 75% PART SPEED

As expected, FIGURE 7 shows that an unstable behavior of the aeroelastic system is expected while approaching the stall line for the 1F2D mode. Especially, dp20 is the least stable operating point. Hence, even if it is not the nearest operating point to stall, we will focus on this operating point for the rest of the study as it is the worst case scenario from a stability point of view on the considered 75% part speed. The 1F3D mode on the other hand remains always stable. FIGURE 8 illustrates the normalized aerodynamic work per unit of surface on the blade pressure and suction sides for the 1F2D mode on dp20 operating point. As mentioned in the previous subsection, one may observe that the most destabilizing area (depicted in red in FIGURE 8) is located around the suction side leading edge shock. The oscillation of the shock due to the blade vibration as well as an appropriate inter blade phase angle are responsible of the energy transfer between the fluid and the structure. However, they are not the only mechanisms inducing flutter at 75% part speed for studied transonic fan.

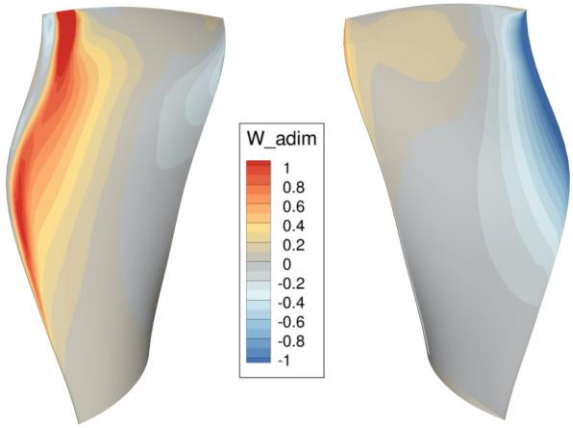

FIGURE 8: AERODYNAMIC WORK ON DP20 OPERATING POINT FOR THE 1F2D MODE

A previous study from the authors [26] showed that acoustic interactions is expected between the fan and the engine intake for the 1F2D mode at 75% part speed near stall. Even if the acoustic description of the case is not the subject of this study and will not be addressed here, we are nevertheless insured that acoustic interactions occur on operating point dp20 for the 1F2D mode and have an impact on the fan stability. Moreover, inlet acoustic propagation does not occur for an isolated operating points, but on the whole compressor map as soon as the acoustic source frequency is above the cut-on frequency [7]. In our case, all the operating points around dp20 operating point are close enough to each other in terms of characteristics (see FIGURE 5) to approximate that the cut-on frequencies of each points are the same. For equivalent working conditions and cut-on frequencies, we thus expect that inlet fan acoustic interactions have approximately the same impact on aeroelastic stability for those operating points. This approximation seems to be confirmed by FIGURE 7 where one can see similar stability results in a neighborhood of dp20 operating point. Since dp20 operating is the least stable according to FIGURE 7 and since acoustic interactions are expected to produce the same effects on all operating points around dp20, this operating point will be considered to apply the coupling strategy with the nonlinear structure in order to find flutter induced LCO. Especially, we will see that even the least stable operating point can be stabilized when taking into account nonlinear friction at blade roots.

4.5 Strong coupling procedure

The strong coupling procedure has been applied using the ROM on dp20 operating point. To do so, five samples of energy level (multiharmonic movement and free frequency) have been extracted from the nonlinear complex mode in vacuum, and used in aeroelastic simulations to evaluate aerodynamic forces. At this point, it should be mentioned that it was not possible to deform the aerodynamic grid for the highest amplitudes as negative cells kept occurring at blade tip shroud gap. Hence, aeroelastic computations were made at lower amplitude values, while resulting aerodynamic forces where brought to the corresponding high amplitude levels using a linearity hypothesis. It does not change the generality of the strong coupling procedure, as it has only been done to bypass the deformation algorithm limitations. The results were used to create a continuous law of aerodynamic forces against the amplitude of movement at tip leading edge on a node called n_{obs}, and compute a new nonlinear complex mode taking into account aerodynamic forces. Several iterations of the strong coupling procedure have been done to assess the so-called aeroelastic nonlinear complex mode convergence. Each aeroelastic computation was run on 112 cores, for a total wall clock time of 7 days per computation. Results of the strong coupling procedure are shown in FIGURE 9 and may be compared to the ones obtained in vacuum. In this figure are plotted the evolution of free frequency and nonlinear damping defined as β/ω against a normalized value of n_{obs} amplitude. The normalization factor comes from an experimentally observed LCO on the studied working conditions: a normalized amplitude of 1 represents the mean stabilized LCO amplitude value observed during experiment. However, the comparison of numerical results with experimental data is beyond the scope of this study and will be addressed in more details in another paper. Especially, the chosen values of friction coefficient or structural natural damping may have an impact on the predicted LCO amplitude.

First, let us discuss about the vacuum case depicted by the darker blue curve in FIGURE 9. This case represents the classical application of nonlinear complex modes using equation (4). It allows one to visualize how the system dynamics changes with respect to the system energy level (*i.e* its vibration amplitude) when no aerodynamic forces are taken into account. For the lowest amplitudes, the system is asymptotically linear as the vibration amplitude is not high enough to trigger friction. In such conditions, the normalized free frequency is approximately equal to the eigen frequency of the corresponding eigen mode. It is not exactly 1 due to the CB reduction, which leads to a small frequency error in comparison to the Full Order Model (FOM). This error is however lower that 0.5% of the FOM free frequency, which will not alter the acoustic inlet reflection properties and hence which is acceptable. Concerning the nonlinear damping for the lowest amplitude values, it approximately equals the linear natural damping of the substructures for stuck conditions, hence resulting in a positive value around 0.05% for the asymptotical linear mode.

When considering results of the strong coupling procedure (depicted by the other curves in FIGURE 9), quick changes are observed on the nonlinear dynamics of the structure from a null amplitude. This numerical artifact has no physical meaning and exists due to the interpolation of aerodynamic forces: since no evaluation of these forces has been provided for a null amplitude, the system is equivalent to the structure in vacuum. This explains why all the nonlinear complex modes start from the same point when the amplitude equals 0. As soon as the amplitude increases, the interpolation law gives non zero aerodynamic forces, which have an impact on the nonlinear complex mode computation: aerodynamic stiffness and damping take place in the system, thus changing the free frequency and the overall nonlinear damping. When using the strong coupling procedure, it then should be kept in mind that true physical meaning is only obtained beyond the first interpolation point (from an amplitude of 0.6 in FIGURE 9 for instance).

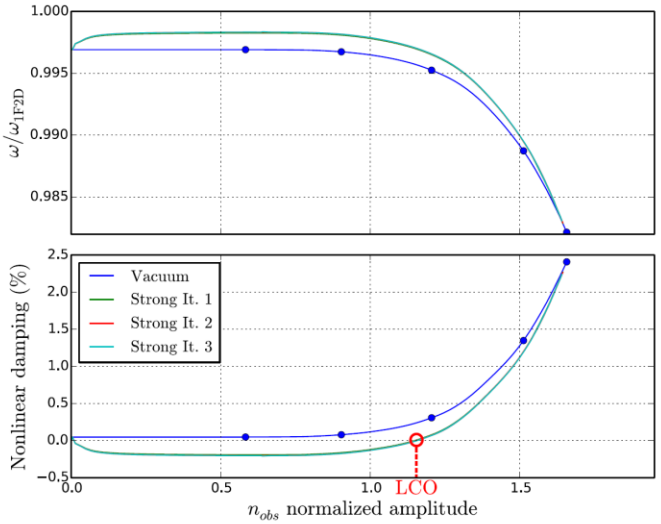

FIGURE 9: APPLICATION OF THE STRONG COUPLING PROCEDURE ON DP20 OPERATING POINT. ●— : EXTRACTION POINTS FROM THE NONLINEAR DYNAMICS IN VACUUM

In spite of some local discrepancies between the curves, especially for small amplitudes whether the coupled or uncoupled cases are considered, each one of them have the same trends with respect to the vibration amplitude. Especially, one may observe the system being softer as the free frequency decreases with increasing values of vibration amplitude. This is due to the activation of friction at high amplitude values, which causes the liberation of some d.o.f at blade roots leading to a less stiff blade disk system. This behavior is typical of mechanical system with friction [27]. The same observations can be made regarding the nonlinear damping. Some discrepancies between the coupled and uncoupled cases are visible, especially for small amplitude values, but the global trends remain the same. With increasing values of vibration amplitude comes increasing values of nonlinear damping as dissipation occurs by dry friction at blade roots. A negative value of nonlinear damping means that the system is self-excited (*i.e* unstable considering equation (2))

while a positive value means the system is damped (*i.e* stable). Hence, the more the system vibrates, the more relative displacements appear at blade roots and thus the more energy is dissipated by friction, leading to a more stable system.

The case in vacuum is always stable, as the nonlinear damping is positive from small amplitude of vibrations. However, the coupled cases are unstable (resp. stable) for normalized amplitude values below (resp. above) 1.2 as the nonlinear damping is negative (resp. positive) in this range of amplitude. The zero damping amplitude (around a normalized value of 1.2) reveals the presence of a stable LCO on the considered dp20 operating point, as lower or higher amplitude values will be respectively accompanied with self-excited or damped dynamics.

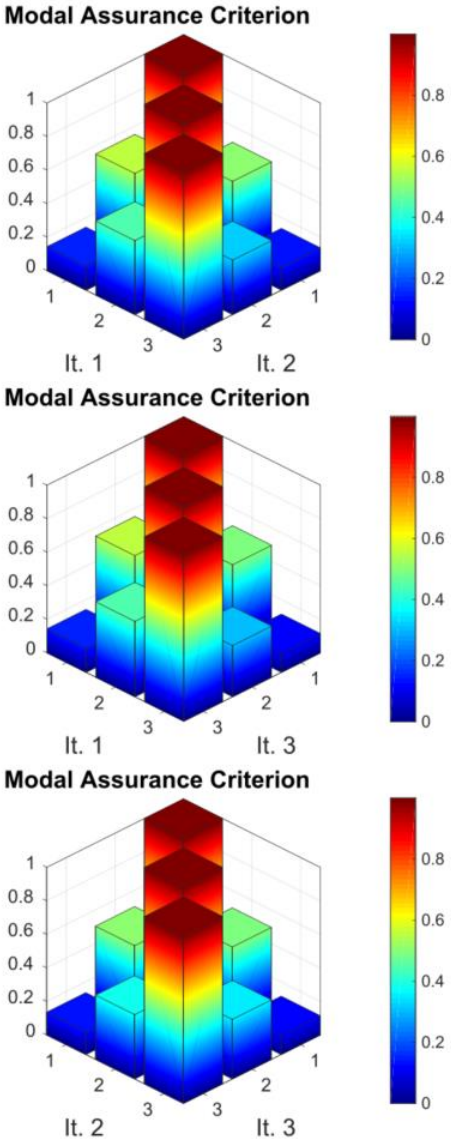

FIGURE 10: MODAL ASSURANCE CRITERION APPLICATION ON THE HARMONICS OF DISPLACEMENT OF PHYSICAL D.O.F ON THE LCO

FIGURE 9 also gives some insights about the convergence of the strong coupling procedure. The depicted number of iterations represents how many times the aerodynamic response has been evaluated to update the nonlinear complex mode (*i.e* how many time the CFD box has been gone through in FIGURE 1). It can be seen from an iteration to another that all the aeroelastic nonlinear complex modes are superimposed. When looking at the LCO especially, which is the point in which we are the most interested, it is predicted at the same amplitude of vibration with the same free frequency, regardless of the number of strong coupling procedure iteration. Thus, the aeroelastic nonlinear complex mode seems to be converged since the first strong coupling iteration. FIGURE 10 allows to get more information about the procedure convergence when it comes to determine the LCO. It represents the Modal Assurance Criterion (MAC) computed between the harmonics of displacement of the predicted LCO on operating point dp20 from a strong coupling iteration to another. The MAC is computed as in equation (12).

$$\mathrm{MAC}(\Phi_1, \Phi_2) = \frac{\left(\Phi_1^H \Phi_2\right)^2}{\left(\Phi_1^H \Phi_1\right)\left(\Phi_2^H \Phi_2\right)} \qquad (12)$$

FIGURE 10 shows that independently of the iteration number, the second harmonic presents similarities in its deformation shape with both harmonics 1 and 3. On the other hand, harmonic 1 and harmonic 3 do not seem to have similar shapes. When looking at the MAC between iterations, one may notice that the displacement topologies remain the same as each harmonic *k* has a MAC above 0.99 from an iteration *i* to an iteration *j*. Some discrepancies may be observed from the MAC values between different harmonics from an iteration to another, especially between harmonics 1 and 2, and harmonics 2 and 3; but it remains of second order. From a design point of view, the strong coupling procedure seems to be converged since the first iteration as the LCO remains the same in terms of vibration amplitude, deflection shape and free frequency at first order.

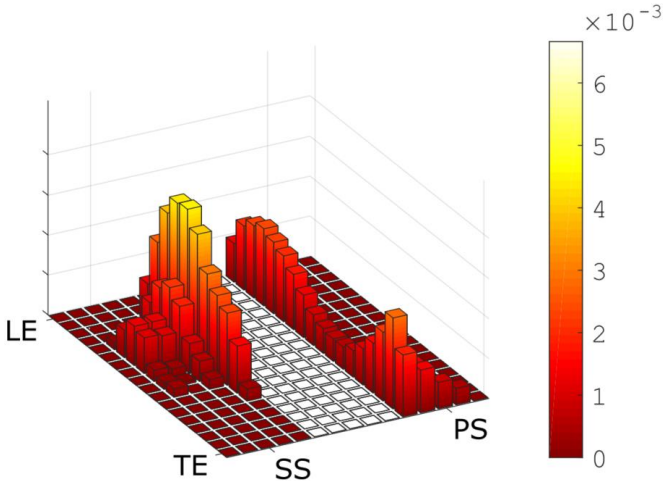

FIGURE 11: ENERGY DISSIPATED (IN JOULE) AT BLADE ROOTS DURING A PERIOD OF VIBRATION OF THE LCO REACHED ON OPERATING POINT DP20

The topology of dissipated energy at flattened blade roots on the LCO is displayed in FIGURE 11. The height of each bars as well as the colormap represents the amount of local dissipated energy at blade roots on the LCO. The white zone in the middle represents the blade location. It appears that dissipation topology differs whether we consider the contact interface on the suction side (SS) or the pressure side (PS). On the suction side, dissipation occurs closer to the leading edge (LE) than the trailing edge (TE). This behavior was expected as the blade has not particular symmetry properties. Dissipation occurs mainly on the top of contact interfaces where an opening of the dovetail joints is expected due to centrifugal forces: as normal contact forces are consequently supposed to be lower than on the other part of the interfaces, saturation of friction forces is reached sooner, giving rise to dissipation.

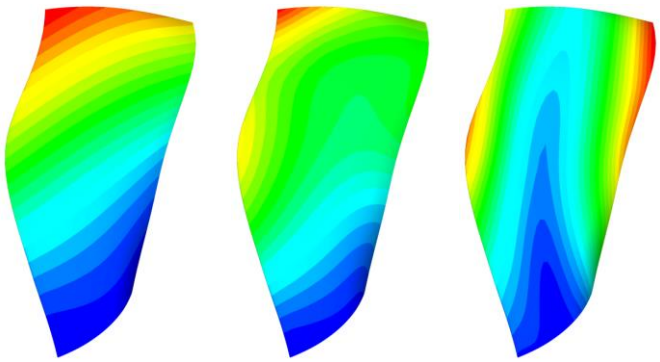

FIGURE 12: MODULE OF HARMONICS DISPLACEMENT ON THE CONVERGED LCO FOR DP20 OPERATING POINT

Lastly, FIGURE 12 illustrates the blade motion on the predicted LCO obtained from the physical degree of freedom kept on the blade skin when creating the ROMs. It can be seen that for the first harmonic, the blade motion keeps its bending topology. It is interesting to see that a torsion deflection shape occur on the third harmonic.

5. CONCLUSION

In this study, a new methodology has been developed for predicting fan blade flutter induced LCOs by taking into account nonlinear friction forces at the blade roots. This methodology allows for an evaluation of the fluid behavior based on the nonlinear dynamics of the structure (such as deformation shape and movement frequency), ensuring that the entire nonlinear aeroelastic system is consistent once convergence is achieved. As a result, it is possible to analyze the dynamics of the aeroelastic system beyond the stability limits predicted for a linear structure. Specifically, this methodology enables us to determine whether the system vibrations will increase exponentially or if stable periodic oscillations (LCO) will occur.

Additionally, dry friction nonlinearities may affect the aeroelastic stability by influencing the inlet fan's acoustic interactions. Since the free vibration frequency can be changed by dry friction, there may be an impact on the open duct's acoustic reflection, which largely depends on the frequency of the acoustic source. The coupling strategy presented in this study accounts for the influence of frequency shifts on the acoustic inlet fan interaction. In a future study, we will examine this effect in more detail.

Lastly, we will compare the methodology outlined in this paper to a previous methodology described by the authors [26] and assess its validity using experimental data.

ACKNOWLEDGEMENTS

The present study has been done thanks to the support of Safran Aircraft Engines.

REFERENCES

[1] Aotsuka, M., Tsuchiya, N., Horiguchi, Y., Nozaki, O., & Yamamoto, K. (2008, January). Numerical simulation of transonic fan flutter with 3D NS CFD code. In Turbo Expo: Power for Land, Sea, and Air (Vol. 43154, pp. 723-734).

[2] Vahdati, M., Simpson, G., & Imregun, M. (2011). Mechanisms for wide-chord fan blade flutter. Journal of Turbomachinery, 133(4).

[3] Aotsuka, M., & Murooka, T. (2014, June). Numerical analysis of fan transonic stall flutter. In Turbo Expo: Power for Land, Sea, and Air (Vol. 45776, p. V07BT35A020). American Society of Mechanical Engineers.

[4] Dong, X., Zhang, Y., Zhang, Y., Zhang, Z., & Lu, X. (2020). Numerical simulations of flutter mechanism for high-speed wide-chord transonic fan. Aerospace Science and Technology, 105, 106009.

[5] Marshall, J. G., & Imregun, M. (1996). A review of aeroelasticity methods with emphasis on turbomachinery applications. Journal of fluids and structures, 10(3), 237-267.

[6] Vahdati, M., Smith, N., & Zhao, F. (2015). Influence of intake on fan blade flutter. Journal of Turbomachinery, 137(8), 081002.

[7] Zhao, F., Smith, N., & Vahdati, M. (2017). A simple model for identifying the flutter bite of fan blades. Journal of Turbomachinery, 139(7), 071003.

[8] Rienstra, S. W., & Hirschberg, A. (2004). An introduction to acoustics. Eindhoven University of Technology, 18, 19.

[9] Sinha, A., & Griffin, J. H. (1983). Friction damping of flutter in gas turbine engine airfoils. Journal of Aircraft, 20(4), 372-376.

[10] Petrov, E. P. (2012). Analysis of flutter-induced limit cycle oscillations in gas-turbine structures with friction, gap, and other nonlinear contact interfaces.

[11] Lassalle, M., & Firrone, C. M. (2018). A parametric study of limit cycle oscillation of a bladed disk caused by flutter and friction at the blade root joints. Journal of Fluids and Structures, 76, 349-366.

[12] Berthold, C., Gross, J., Frey, C., & Krack, M. (2021). Development of a fully-coupled harmonic balance method and a

refined energy method for the computation of flutter-induced Limit Cycle Oscillations of bladed disks with nonlinear friction contacts. Journal of Fluids and Structures, 102, 103233.

[13] Laxalde, D., & Thouverez, F. (2009). Complex non-linear modal analysis for mechanical systems: Application to turbomachinery bladings with friction interfaces. Journal of sound and vibration, 322(4-5), 1009-1025.

[14] Joannin, C., Chouvion, B., Thouverez, F., Mbaye, M., & Ousty, J. P. (2016). Nonlinear modal analysis of mistuned periodic structures subjected to dry friction. Journal of Engineering for Gas Turbines and Power, 138(7).

[15] Nayfeh, A. H., & Balachandran, B. (2008). Applied nonlinear dynamics: analytical, computational, and experimental methods. John Wiley & Sons.

[16] Cambier, L., Heib, S., & Plot, S. (2013). The Onera elsA CFD software: input from research and feedback from industry. *Mechanics & Industry*, *14*(3), 159-174.

[17] Smith, B. (1994). A near wall model for the k-l two equation turbulence model. In Fluid Dynamics Conference (p. 2386).

[18] Roe, P. L. (1981). Approximate Riemann solvers, parameter vectors, and difference schemes. Journal of computational physics, 43(2), 357-372.

[19] Van Albada GD, Van Leer B, Roberts WW. A comparative study of computational methods in cosmic gas dynamics. Astron Astrophys 1982;108:76-84.

[20] Donea, J., Giuliani, S., & Halleux, J. P. (1982). An arbitrary Lagrangian-Eulerian finite element method for transient dynamic fluid-structure interactions. Computer methods in applied mechanics and engineering, 33(1-3), 689-723.

[21] May, M., Mauffrey, Y., & Sicot, F. (2011). Numerical flutter analysis of turbomachinery bladings based on time-linearized, time-spectral and time-accurate simulations. Proceedings" IFASD 2011".

[22] Gross, J., Krack, M., & Schoenenborn, H. (2018). Analysis of the effect of multirow and multipassage aerodynamic interaction on the forced response variation in a compressor configuration—Part II: Effects of additional structural mistuning. Journal of Turbomachinery, 140(5), 051005.

[23] Craig Jr, R. R., & Bampton, M. C. (1968). Coupling of substructures for dynamic analyses. AIAA journal, 6(7), 1313-1319.

[24] Nacivet, S., Pierre, C., Thouverez, F., & Jézéquel, L. (2003). A dynamic Lagrangian frequency–time method for the vibration of dry-friction-damped systems. Journal of Sound and Vibration, 265(1), 201-219.

[25] Lemoine, E. (2021). Approche couplée pour l'étude du contact sous chargement dynamique vibratoire: application à l'usure par fretting du contact aube-disque (Doctoral dissertation, Lyon).

[26] Ombret, N., de Pret, M., Dugeai, A., Thouverez, F., Blanc, L., & Berthelon, T. (2021, June). Investigation of a methodology for describing Fan Blade Flutter limitations induced by non-linear friction at blade roots. In COMPDYN 2021.

[27] Charleux, D., Gibert, C., Thouverez, F., & Dupeux, J. (2006). Numerical and experimental study of friction damping blade attachments of rotating bladed disks. International Journal of Rotating Machinery, 2006.